

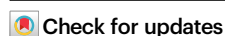


Atomically precise ligand engineering of gold nanoparticles via interphase mass transfer

Received: 17 March 2025

Accepted: 26 December 2025

Published online: 12 January 2026



Bihan Zhang^{1,7}, Feng Xiao^{2,7}, Xiaorong Song³, Moshuqi Zhu⁴✉, Qiaofeng Yao^{5,6}✉ & Jianping Xie^{1,4}✉

Precise surface engineering of gold nanoclusters (Au NCs) is critical for bioimaging. However, conventional methods often compromise the structural integrity of Au NCs or result in uncontrolled ligand distribution due to rapid reaction kinetics and etching side reactions. Herein, we develop an interphase-assisted ligand exchange method, which leverages mass transfer resistance between immiscible phases to precisely control the mass transfer of ligands. This approach significantly suppresses side etching while maintaining exchange kinetics, enabling high-yield, structure-preserving substitution of diverse thiol ligands on Au NCs. By systematically introducing *p*-aminothiophenol (*p*-ATP) ligands, we reveal that increasing *p*-ATP density on Au₂₅ NCs shifts their biodistribution in female BALB/c nude mice from liver and spleen to kidneys, highlighting the tunability of organ targeting through ligand engineering. The methodology developed here not only boosts the surface engineering to molecular resolution, but also provides a platform for studying ligand effects of metal nanomaterials at the same resolution.

The precise surface engineering of nanoparticles (NPs) has emerged as a pivotal strategy in advancing bioimaging technologies, particularly due to the crucial role surface ligands play in mediating the interaction of NPs with biological systems^{1–4}. Fine-tuning the surface chemistry of NPs not only enhances their stability and biocompatibility but also governs their biodistribution, cellular uptake, and clearance pathways, which are key determinants in imaging performance and clinical translation^{5–9}. However, achieving atomically precise ligand engineering remains a formidable challenge, primarily due to the intrinsic difficulties associated with the synthesis, characterization, and stability of conventional NPs at the atomic level.

The heterogeneity of nanoparticle surfaces and the dynamic nature of surface-bound ligands further complicate efforts to achieve controlled functionalization, impeding progress in nanoscale-to-atomic-level surface engineering^{10–12}.

Gold nanoclusters (Au NCs), a unique subclass of gold nanoparticles, have garnered significant interest in bioimaging due to their distinct physicochemical properties^{13–15}. Distinguished by their ultra-small size (< 3 nm), Au NCs possess molecule-like properties, including discrete electronic structures and near-infrared II (NIR-II) photoluminescence^{10,16,17}, which make Au NCs particularly suitable for bio-imaging, where deep tissue penetration, minimal autofluorescence,

¹Department of Chemical and Biomolecular Engineering, National University of Singapore, Singapore, Singapore. ²Guangdong Provincial Key Laboratory of Advanced Biomaterials, Shenzhen Key Laboratory of Smart Healthcare Engineering, Department of Biomedical Engineering, Southern University of Science and Technology, Shenzhen, Guangdong, PR China. ³MOE Key Laboratory for Analytical Science of Food Safety and Biology & State Key Laboratory of Photocatalysis on Energy and Environment, College of Chemistry, Fuzhou University, Fuzhou, China. ⁴Joint School of National University of Singapore and Tianjin University, International Campus of Tianjin University, Binhai New City, Fuzhou, PR China. ⁵Key Laboratory of Organic Integrated Circuits, Ministry of Education & Tianjin Key Laboratory of Molecular Optoelectronic Sciences, Department of Chemistry, School of Science, Tianjin University, Tianjin, China. ⁶Collaborative Innovation Center of Chemical Science and Engineering (Tianjin), Tianjin, China. ⁷These authors contributed equally: Bihan Zhang, Feng Xiao. ✉ e-mail: zhumoshuqi@tju.edu.cn; qfyao@tju.edu.cn; chexiej@nus.edu.sg

and high contrast are paramount. However, this size regime presents a fundamental challenge, that is the high surface-area-to-volume ratio makes their biological behavior exquisitely sensitive to the chemical nature of the protecting ligand shell. Their ultimate fate in a biological system—from biodistribution and clearance to biocompatibility and cellular interactions—is dictated largely by the surface ligands rather than the inert gold core^{15,18–22}. Therefore, while the unique optical properties of Au NCs are highly attractive for bioimaging, unlocking this potential is fundamentally a problem of surface chemistry. Without methods for achieving unprecedented control over ligand composition, their behavior remains difficult to predict and optimize, hindering their rational design for specific biological applications.

One of the most distinctive advantages of Au NCs is their well-defined atomic structure, often referred to as $[Au_n(L)_m]^q$, where n , m , and q denote the number of gold atoms, ligands (L), and net charge, respectively^{23–25}, provide an ideal platform for investigating the relationship between surface chemistry and bioimaging performance. However, the practical realization of precision-controlled surface engineering of NCs remains an unmet challenge. While various methods have been developed to modify the ligand shell of NCs^{26,27}, each approach presents significant limitations. Direct synthesis is laborious and time-consuming, with unpredictable final products due to the complex fundamentals of NCs' synthesis^{28–30}. In contrast, ligand exchange offers a more accessible and feasible route for engineering protecting shell of Au NCs, as the size of parent Au NCs holds a good chance to be retained³¹. However, it turns out difficult to precisely control ligand distribution in ligand exchange reaction most probably due to the rapid reaction kinetics³². Moreover, maintaining the structural integrity of Au NCs during ligand exchange also faces some problems^{33–35}, as free ligands can also induce etching reaction, which is a major side reaction compromising the structural and thus property stability of Au NCs^{36,37}. For bioimaging applications of Au NCs, preserving the structure is crucial to retain their NIR-II emission characteristics, as the emission wavelength is closely tied to the structural configuration of the NCs^{38,39}. As a result, development of a controllable, structure-preserving ligand exchange technique remains an unmet need, impeding deeper insights into the ligand effects on bioimaging of Au NCs.

In this study, we develop an interphase mass transfer strategy to understand and realize atomically precise ligand exchange on the surface of Au NCs. This interphase mass transfer method depends on a diffuse phase boundary established by two partially miscible solvents, like ethyl acetate (EA) and water. Through the mass transfer barrier established by this phase boundary, we are able to program the concentration of free ligands in a mild and sustainable way, which can significantly mitigate the etching side reaction induced by concentrated free thiols. By this way, we achieve precise, high-yield, and structure-preserving ligand exchange of thiolate-protected Au NCs. Using $Au_{25}(p\text{-MBSA})_{18}$ NCs as a model⁴⁰, where *p*-MBSA denotes *para*-mercaptobenzenesulfonic acid, we performed ligand exchanges with a variety of thiol ligands, including *para*-mercaptobenzoic acid (*p*-MBA), 3-mercaptopropionic acid (MPA), and 6-mercaptohexanoic acid (MHA), among others. The interphase-assisted ligand exchange—where Au NCs are dispersed in an aqueous phase and free incoming ligands in an organic EA phase—enables biased control over the kinetics of ligand exchange reactions and side etching reactions. Remarkably, this interphase mass transfer method slows down the kinetics of side etching reaction by 60-fold, while exerting marginal influence on the ligand exchange kinetics. This provides a good mechanism to minimize the side ligand etching reaction during the ligand exchange process, maintaining a high ligand exchange yield of 94% while preserving the structural integrity of parent Au_{25} NCs. Moreover, the mild ligand exchange kinetics sustained by the interphase mass transfer strategy provides a precise control over the extent of ligand exchange on the surface of Au NCs, as well as a good

versatility toward a wide range of thiol ligands with varied ligand body structures and functional groups. Leveraging this approach, we successfully synthesize a series of $-SO_3H$ and $-NH_2$ co-protected Au_{25} NCs with customizable ligand distributions. Intriguingly, the delicately customized surface charge density on as-synthesized bi-thiolate-protected Au NCs makes possible their discriminated in-vivo accumulation profiles in different mammalian organs. These findings reveal the critical role of surface ligands in bio-imaging at the atomic level, highlighting the potential of our method for advancing ligand engineering chemistry from nanoscale to atomic resolution.

Results

Understanding the ligand exchange reaction

Developing an advanced ligand exchange method requires a deep understanding of the ligand exchange mechanism. It is well-established that excess free ligands in solution effectively initiate ligand exchange on the surface of Au NCs^{33,41}. However, excess ligands also accelerate the undesirable etching of the cluster cores, particularly in the presence of dissolved oxygen^{42,43}. This etching reaction compromises both the monodispersity and structural integrity of parent Au NCs, representing a major side reaction against precise ligand engineering (Fig. 1).

It has now become clear that suppression of the etching side reaction kinetics should be conducive to improving the yield of the desired ligand exchange product. To better elucidate the factors driving etching reaction, we formulated its rate by Eq. (1):

$$\frac{d[Au\ NCs]_{Etch}}{dt} = k_{Etch}[Au\ NCs]^x[SR]^y \quad (1)$$

where the k_{Etch} is the rate constant, and x and y are the reaction orders with respect to Au NCs and thiolate ligands (SR), respectively. By determining the reaction orders, we aimed to clarify the roles that Au NCs and free ligands play in the etching reactions. To quantify this, we monitored the absorbance of Au_{25} NCs at 698 nm, which is a good index of cluster concentration $[Au\ NCs]$ based on the Beer-Lambert's law, during etching reaction under varying concentrations of $Au_{25}(p\text{-MBSA})_{18}$ and free ligands. For this analysis, we strategically chose *p*-MBA as the model ligand; its moderate reactivity induces a measurable etching rate, providing a clear kinetic signature that can be accurately quantified. By taking the logarithmic form of Eq. (1), we can have Eq. (2) below, in which the left-hand-side term can be obtained by differentiating the absorbance data over time (the detailed calculation process can be found in Supplementary Information).

$$\ln\left(-\frac{d[Au\ NCs]_{Etch}}{dt}\right) = \ln k_{Etch} + x \ln[Au\ NCs] + y \ln[SR] \quad (2)$$

By plotting the $\ln(-d[Au\ NCs]_{Etch}/dt)$ against $\ln[Au\ NCs]$ (in excess SR) and $\ln[SR]$ (in excess Au NCs), we are able to deduce the x and y values, respectively. As shown in Fig. 2a and Supplementary Fig. 1, a reaction order of 1.8 for free ligands and 0.04 for Au NCs, i.e., $y_{Etch} = 1.8$ and $x_{Etch} = 0.04$, can be deduced. This result indicates that etching reaction is highly sensitive to ligand concentration, and a minor change in the concentration of ligand can induce significant changes in etching reaction rate.

By similar way, we investigated the dependence of ligand exchange reaction rate on the concentration of free thiol ligands. The rate of ligand exchange reaction can be modeled by Eq. (3).

$$\ln\left(-\frac{d[Au\ NCs]_{LE}}{dt}\right) = \ln k_{LE} + x \ln[Au\ NCs] + y \ln[SR] \quad (3)$$

By calculating the reaction order for ligands in the exchange reaction (Fig. 2b, see Supplementary Information for calculation

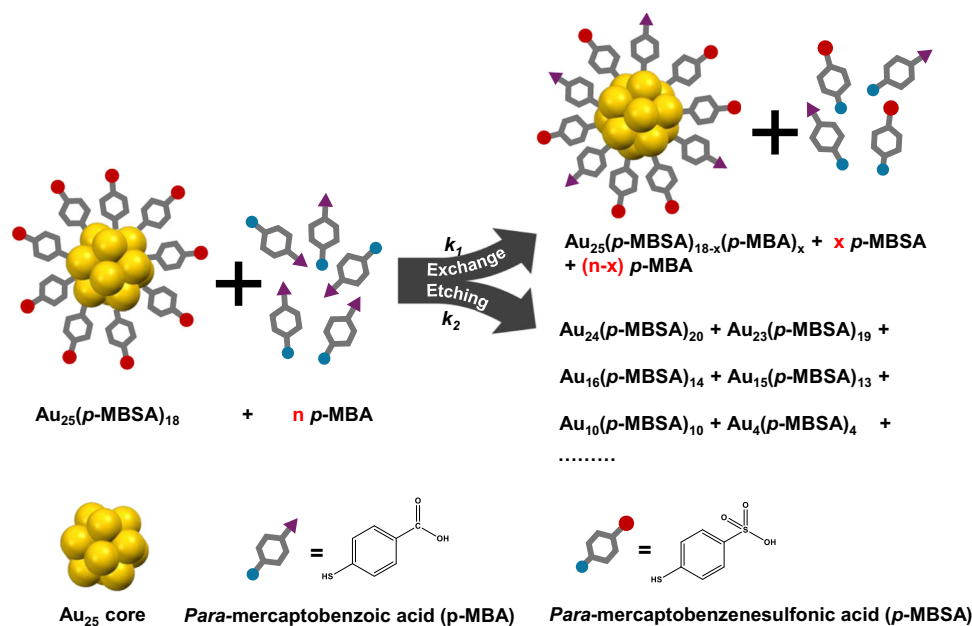


Fig. 1 | Schematic illustration of competing ligand exchange and etching reactions between Au NCs with thiols. *Para*-mercaptobenzoic acid (*p*-MBA) and *para*-mercaptobenzenesulfonic acid (*p*-MBSA) are employed as model ligands.

details), we determined it to be 0.3 (i.e., $y_{LE} = 0.3$) substantially lower than that for etching reaction. The vastly different rate dependence of etching and ligand exchange reactions on $[\text{SR}]$ affords a good mechanism to fine modulate the reaction kinetics of parent Au_{25} NCs with incoming free thiols, selectively suppressing the undesired side etching reaction. Specifically, delicately reducing ligand concentration can slow down the rate of etching reaction significantly, while much less influential to the rate of ligand exchange reaction. Therefore, by properly lowering the concentration of free thiol ligands and supplying them in a sustainable manner, we can achieve high-yield ligand exchange with minimized side etching reaction, thereby maintaining the structural integrity and monodispersity of parent Au_{25} NCs.

Design of interphase-assisted ligand exchange method

Based on the above quantitative understandings on the $[\text{SR}]$ dependence of reaction kinetics, we hypothesize that a delicate control over the $[\text{SR}]$ can become possible via an interphase mass transfer method. We accommodated the $\text{Au}_{25}(\text{p-MBSA})_{18}$ and incoming free thiol ligands (e.g., *p*-MBA) in water and organic phases (Fig. 2c–d), respectively. The selection of two partially miscible phases, like water-EA in this prototype case, is critical in our methodological design, as a partially miscible interphase region can be established between these two phases, implementing a notable yet not too high mass transfer barrier to the diffusion of free thiols and Au_{25} NCs. Upon mixing of water and EA phases, both free ligands and Au NCs diffuse toward the miscible interphase region, in which the reactions between free ligands and Au NCs actually take place. By this way, the concentration of free thiol ligand can be controlled at a properly low level, and the organic phase can serve as a reservoir of free thiol ligands, assuring a constant and stable supply of free thiol ligands upon consumed by ligand exchange reactions. Such delicate and sustainable supply of free thiol ligands can sufficiently drive the ligand exchange reaction while minimizing the side etching reaction. As a result, a high-yield, high monodispersity, structure-preserving ligand exchange reaction is expectable between the original $\text{Au}_{25}(\text{p-MBSA})_{18}$ NCs and *p*-MBA ligands.

To optimize this interphase-assisted ligand exchange strategy, it is essential to understand the key factors governing ligand diffusion between the two phases. The diffusion flux of free ligands can be

described by the simplified Fick's first law (Eq. (4)):

$$N_{\text{SR}} = \frac{D}{\Delta z} (C_{\text{SR1}} - C_{\text{SR2}}) \quad (4)$$

where N_{SR} is the diffusion flux of free ligands (SR); Δz represents the distance along the diffusion path; C_{SR1} and C_{SR2} are the ligand concentrations at the starting and ending points along the diffusion pathway, and D is the diffusion coefficient. This equation highlights that the diffusion rate is primarily governed by the diffusion coefficient D , which can be expressed using the Wilke-Chang equation (Eq. (5)):

$$D = 7.4 \times 10^{-15} (\varphi M)^{0.5} \frac{T}{\mu V^{0.6}} \quad (5)$$

Here, φ is the association factor of the solvent; M is the molecular weight of the solvent; T is the absolute temperature; μ is the viscosity of the solvent, and V is the molar volume of the solute at its boiling point.

Among these variables, the viscosity (μ) of the solvent plays a crucial role, as temperature and molar volume remain constant under our experimental conditions, and the molecular weight (M) has a relatively small impact due to its low exponential power (0.5). Additionally, the association factor φ , ranging from 1 for non-polar solvents to ~ 2.6 for highly associated solvents (like water), exerts only a moderate influence as it is also subject to a power of 0.5. Thus, the viscosity of the solvent emerges as a dominant factor in controlling the diffusion coefficient D . Viscosity is influenced by the interactions between solvent molecules, such as hydrogen bonding, dipole-dipole interactions, and van der Waals forces, which are more prevalent in solvents with high polarity. Therefore, selecting a solvent with appropriate polarity and viscosity is essential for optimizing the diffusivity of free thiol ligands in this two-phase ligand exchange reaction.

Beyond physical solvent properties, the ligand's charge state, governed by the aqueous phase pH, offers a powerful chemical handle to control the reaction. We investigated the pH effects by performing the exchange reaction between $\text{Au}_{25}(\text{p-MBSA})_{18}$ and *p*-MBA at pH 5, 7, and 9, respectively. The results (Supplementary Fig. 2) show a strong

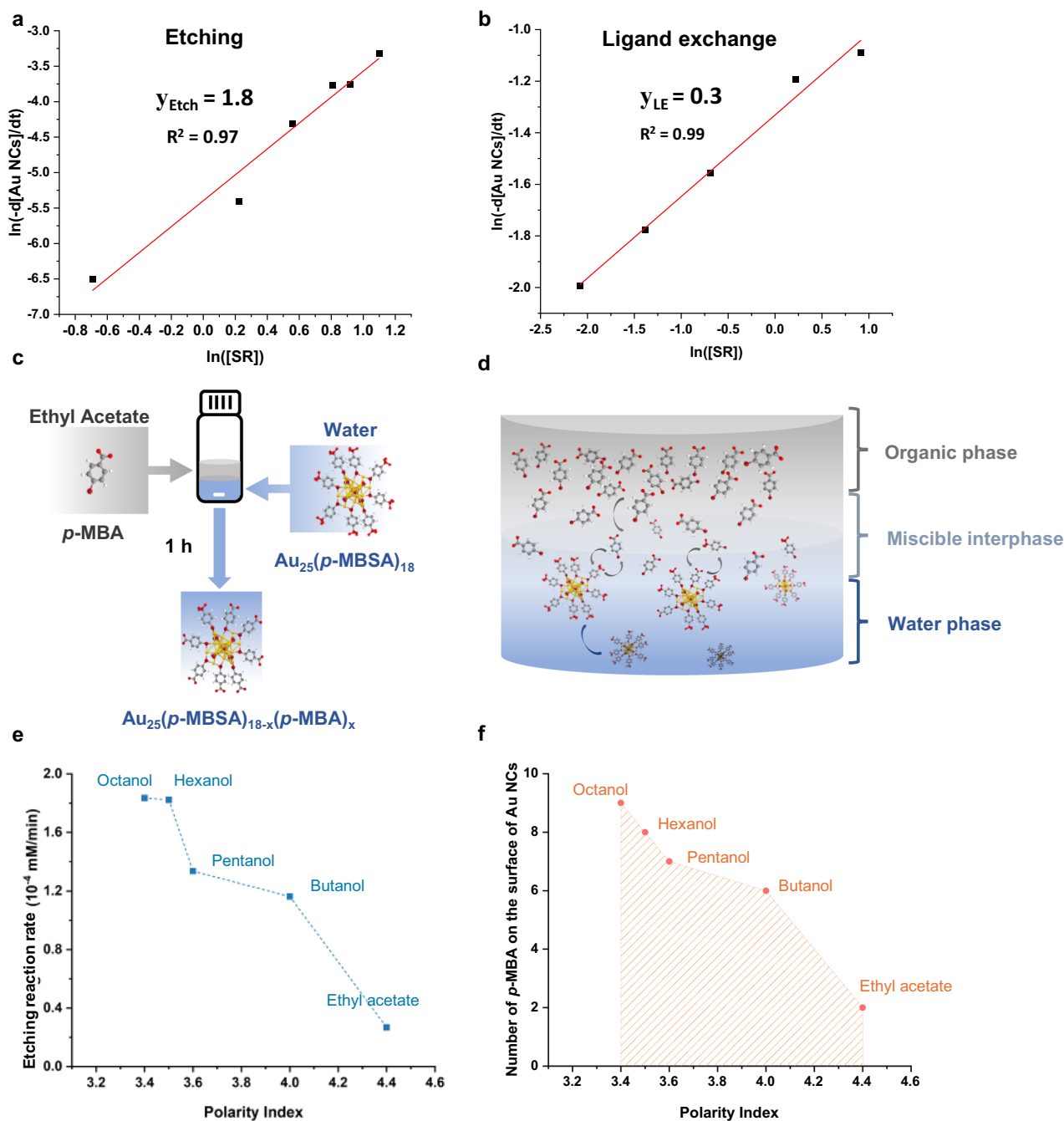


Fig. 2 | Design of the interphase-assisted ligand exchange method. **a** Linear fit of $\ln(-d[\text{Au NCs}]/dt)$ against $\ln([\text{SR}])$ to determine the reaction order of ligands (y_{Etch}) in the etching reaction. **b** Linear fit of $\ln(-d[\text{Au NCs}]/dt)$ against $\ln([\text{SR}])$ to determine the reaction order of ligands (y_{LE}) in the ligand exchange reaction. **c** Schematic representation of the interphase-assisted ligand exchange setup. **d** Schematic illustration of the mechanism governing interphase-assisted ligand

exchange reactions. **e** Comparison of etching reaction rate across interphase-assisted ligand exchange reactions with different organic phases. **f** Comparison of ligand exchange in interphase-assisted ligand exchange reactions with varying organic phases. All experiments were conducted with Au NCs at a concentration of 0.025 mM unless otherwise indicated.

pH dependence, where negligible exchange occurred at pH 5, while the number of incorporated *p*-MBA ligands increased to -1 at pH 7 and -2 at pH 9. This trend is rationalized by the protonation state of the incoming *p*-MBA (pKa -4.5). At pH 5, its carboxylic groups are extensively in neutral form and favor the organic phase, limiting its availability in the interphase regime where ligand exchange reactions occur. Conversely, at higher pH, the deprotonated -COO^- groups become more hydrophilic, increasing its concentration at the water-EA interphase and accelerating the ligand exchange reactions. Given this significant influence, and to achieve a moderate and controllable rate

of interphase-assisted ligand exchange, we standardized the aqueous phase at a buffered pH of 7.0 for all subsequent experiments.

To experimentally verify our hypothesis, we carried out the reactions between $\text{Au}_{25}(\text{p-MBSA})_{18}$ NCs and free *p*-MBA ligands in water-organic two-phase systems with the polarities of organic phase varied from 3.4 to 4.4 (i.e., octanol, hexanol, pentanol, butanol, and EA). In each case, *p*-MBA ligands were dissolved in the organic phase while Au_{25} NCs were dispersed in the aqueous phase. We evaluated both etching and ligand exchange reactions in aforementioned water-organic two-phase systems (calculation details and the cluster species

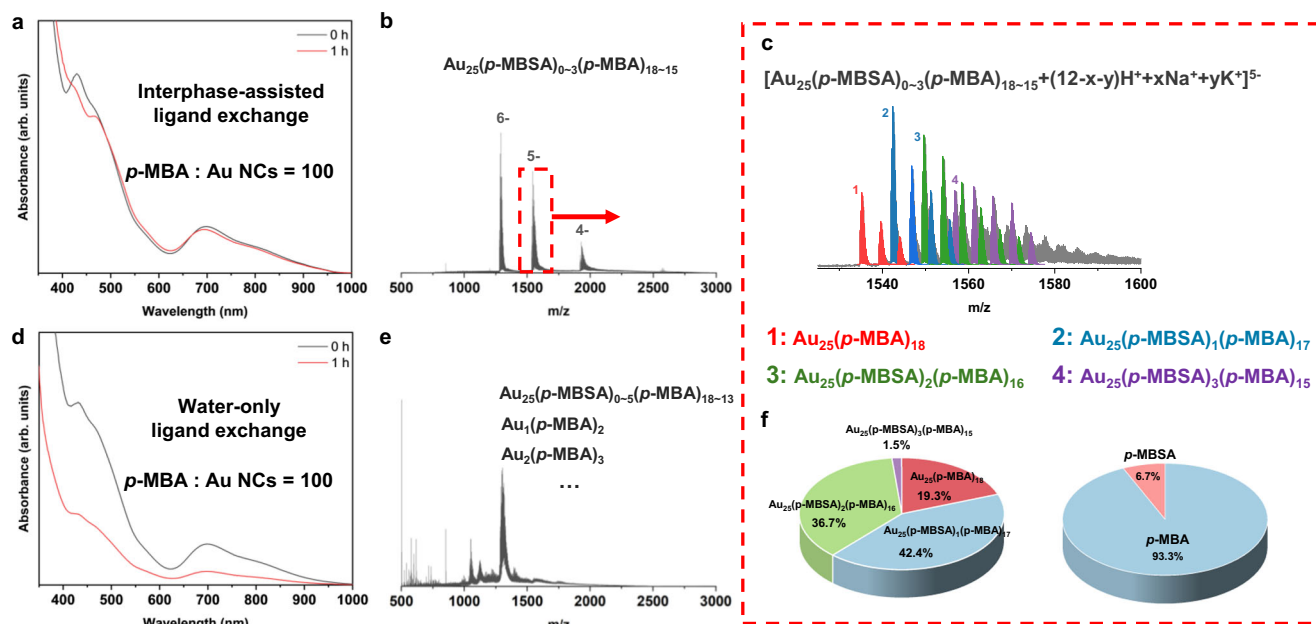


Fig. 3 | Comparison of ligand exchange reactions in interphase-assisted and water-only single-phase systems with high ligands concentration. **a** UV-vis absorption spectra and **b** ESI-MS spectra of Au NCs after 1 h ligand exchange reaction in the interphase-assisted system with a molar ratio of *p*-MBA to Au₂₅(*p*-MBSA)₁₈ = 100: 1. Enlarged and detailed ESI-MS analysis of the signal peak (red rectangle) in **b** is presented in **c** and **f**. 0.025 mM of Au₂₅(*p*-MBSA)₁₈ is dissolved in aqueous phase at pH 7, while 2.5 mM of *p*-MBA is dissolved in EA phase. **d** UV-vis

absorption spectra and **e** ESI-MS spectra of Au NCs after 1 h ligand exchange reaction in the water-only single-phase system under the same ligand and cluster concentration conditions. **c** Detailed identification of Au₂₅(*p*-MBSA)_{18-n}(*p*-MBA)_n species in ESI-MS spectrum of the interphase-assisted ligand exchange reaction, with **f** corresponding Au₂₅(*p*-MBSA)_{18-n}(*p*-MBA)_n species and ligand species (i.e., *p*-MBA and *p*-MBSA) compositional analyses, highlighting the effectiveness of the interphase-assisted ligand exchange method.

identification can be found in Supplementary Information and Supplementary Figs. 3–7). The results (Fig. 1e) show that increasing the polarity of the organic phase leads to a significant decrease in etching reaction rate. This observation supports our hypothesis that solvents with higher polarity retard the diffusion of free thiol ligands, thereby slowing down the etching reactions. In the meantime, a slower diffusion can lead to a lower effective concentration of ligand, which can be seen from Fig. 1f. If that the organic solvent with higher polarity give rise to lower surface coverage by the incoming ligand.

Among the solvents tested, the water-EA system demonstrated optimal performance, reducing the etching rate by more than 68-fold, from 1.11×10^{-1} to 1.61×10^{-3} mM Au NCs/h, compared to the water-only single-phase ligand exchange reaction (Supplementary Fig. 8). In contrast, ligand exchange in the water-EA system exhibited only a 5.5-fold decrease in *p*-MBA coverage—from 11% in the water-only system to 2% in the water-EA system (Supplementary Figs. 9–11), indicating that ligand exchange reaction was preserved despite the significant suppression of etching reaction. This stark contrast highlights that the mass transfer resistance made possible by the water-EA two-phase design effectively passivates the etching reaction while exerting less impact on the ligand exchange reaction.

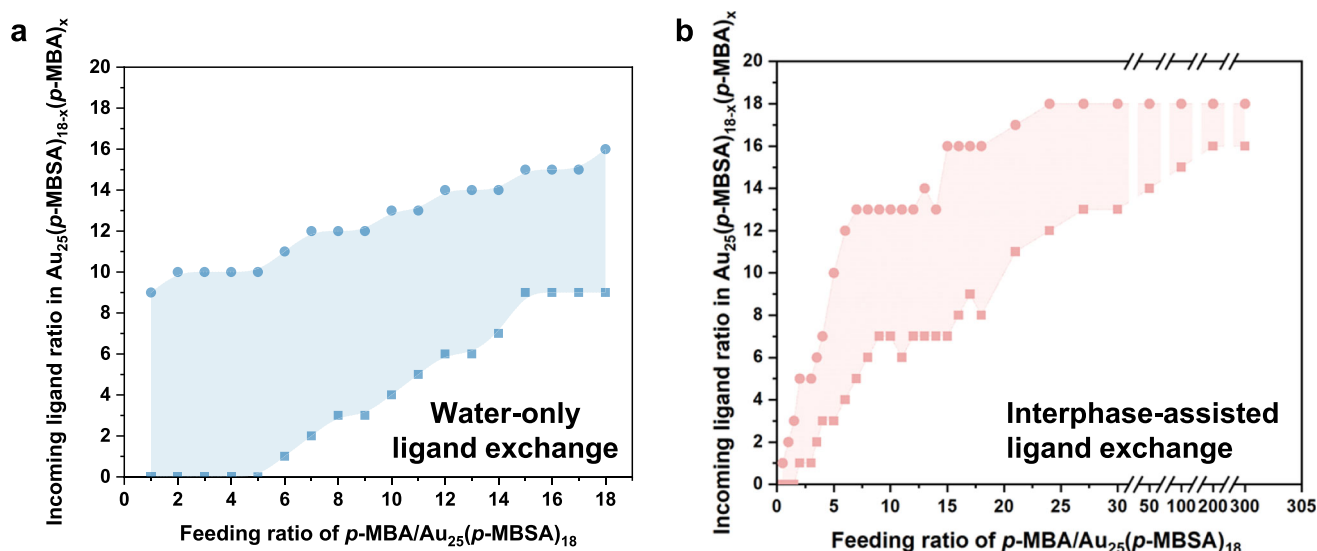
To further validate that the ligand exchange occurs predominantly within the miscible interphase region, we introduced positively charged counterions, trimethylphenylammonium chloride (TPAC) and tributylmethylammonium chloride (TMAC), into the water phase to enhance the solubility of negatively charged Au₂₅(*p*-MBSA)₁₈ within the interphase region. Our experimental results confirmed that both TPAC and TMAC facilitated the ligand exchange process in two-phase reactions, significantly improving the reaction kinetics compared to the bare EA-water system (Supplementary Fig. 12). Specifically, compared to the bare water-EA system which yielded minimal exchange ($n \approx 0-1$), adding TMAC or TPAC increased the extent of *p*-MBA incorporation to distributions of $n = 0-5$ and $n = 0-6$, respectively. Notably, the superior efficacy of TPAC is likely due to favorable

π - π stacking interactions between its phenyl group and the incoming *p*-MBA ligand, further facilitating the reaction at the cluster surface. This compelling evidence together with pH effect we discussed before identified that the miscible interphase is indeed the primary reaction locus, and that our method allows for tunable control by modulating the concentration of either the free ligand (via solvent or pH) or the nanocluster (via phase-transfer catalysts) within this critical region.

Interphase-assisted ligand exchange reaction

To demonstrate the efficacy of this interphase-assisted ligand exchange method in precisely displacing surface thiolate ligands in high yield and purity, we first conducted the ligand exchange reaction in large excess of incoming *p*-MBA ligands. A 100:1 molar ratio of *p*-MBA to Au₂₅(*p*-MBSA)₁₈ was applied in both the interphase-assisted and water-only single-phase ligand exchange systems. The UV-vis absorption spectra (Fig. 3a, d) unambiguously manifest a superior ability of the interphase-assisted ligand exchange method to preserve the structure of parent Au NCs. After 30 min of ligand exchange reaction, approximately 94% of the Au₂₅(*p*-MBSA)₁₈ remained intact in the two-phase system (Fig. 3a), whereas only about 34% persisted in the single-phase system, underscoring a severe etching reaction occurred in the latter system (Fig. 3d).

In order to shed molecule-level light on the ligand exchange reaction, we carried out electrospray ionization mass spectrometry (ESI-MS) analyses in both interphase-assisted and single-phase systems. As shown in Fig. 3b, e, the ESI-MS spectrum acquired in interphase-assisted system displays clean and monodispersed cluster peaks, while that recorded in single-phase system shows messy and polydispersed cluster peaks, closely resembling those of the etching reaction products⁴³ (species analysis of single-phase ligand exchange reaction can be found in Supplementary Fig. 13). A detailed species analysis of the interphase-assisted ligand exchange product is illustrated in Fig. 3c, f. All observed cluster peaks can be assigned to four different clusters, i.e., Au₂₅(*p*-MBSA)_{18-n}(*p*-MBA)_n ($n = 0-3$). For easy



p -MBA : Au NCs	Interphase-assisted ligand exchange	Water-only ligand exchange
1:1	$\text{Au}_{25}(\text{p-MBSA})_{18-16}(\text{p-MBA})_{0-2}$	$\text{Au}_{25}(\text{p-MBSA})_{18-9}(\text{p-MBA})_{0-9}$
2:1	$\text{Au}_{25}(\text{p-MBSA})_{17-13}(\text{p-MBA})_{1-5}$	$\text{Au}_{25}(\text{p-MBSA})_{18-8}(\text{p-MBA})_{0-10}$
4:1	$\text{Au}_{25}(\text{p-MBSA})_{15-11}(\text{p-MBA})_{3-7}$	$\text{Au}_{25}(\text{p-MBSA})_{18-8}(\text{p-MBA})_{0-10}$
6:1	$\text{Au}_{25}(\text{p-MBSA})_{14-6}(\text{p-MBA})_{4-12}$	$\text{Au}_{25}(\text{p-MBSA})_{17-7}(\text{p-MBA})_{1-11}$
9:1	$\text{Au}_{25}(\text{p-MBSA})_{11-5}(\text{p-MBA})_{7-13}$	$\text{Au}_{25}(\text{p-MBSA})_{15-6}(\text{p-MBA})_{3-12}$
.....

Fig. 4 | Precise control of ligand exchange extent using the interphase-assisted approach. Comparison of ligand distribution on the surface of Au_{25} NCs after ligand exchange in **a** water-only single-phase and **b** interphase-assisted systems with varying p -MBA: $\text{Au}_{25}(\text{p-MBSA})_{18}$ ratios. The bottom chart displays the

molecular formulas of $\text{Au}_{25}(\text{p-MBSA})_{18-n}(\text{p-MBA})_n$ obtained from the interphase-assisted and water-only single-phase ligand exchange reactions at low p -MBA: $\text{Au}_{25}(\text{p-MBSA})_{18}$ ratios (< 9). The concentration of $\text{Au}_{25}(\text{p-MBSA})_{18}$ and aqueous pH used in both systems are 0.025 mM and 7, respectively.

identification, cluster peaks corresponding to individual n values are marked by different colors in the ESI-MS spectrum (Fig. 3c). The isotope patterns of each species are shown in the Supplementary Fig. 14. We then calculated the percentage of each cluster in the ligand exchange product based on their peak intensities in ESI-MS spectrum. $\text{Au}_{25}(\text{p-MBSA})_1(\text{p-MBA})_{17}$ is the most abundant species and constitutes 42.4% of all Au_{25} NCs. The second most abundant species is measured to be $\text{Au}_{25}(\text{p-MBSA})_2(\text{p-MBA})_{16}$ with a population of 36.7%, and the totally exchanged species, i.e., $\text{Au}_{25}(\text{p-MBA})_{18}$ takes the rest 20% population. That is p -MBA exchanged over 90% p -MBSA on the surface of $\text{Au}_{25}(\text{p-MBSA})_{18}$, transferring the $-\text{SO}_3^-$ covered Au_{25} NCs to $-\text{COO}^-$ protected one. These findings validate our hypothesis that controlling free ligand concentration through interphase mass transfer approach can effectively suppress etching reactions, promoting high-yield ligand-exchange reactions.

Beyond its ability to suppress the etching reaction, the interphase-assisted method is also able to offer precise control over the ligand exchange extent. We explored a wide range of p -MBA to $\text{Au}_{25}(\text{p-MBSA})_{18}$ ratios in the interphase-assisted system, and obtained ligand-

exchanged $\text{Au}_{25}(\text{p-MBSA})_{18-n}(\text{p-MBA})_n$ in a whole spectrum of $n = 0 - 18$ (Fig. 4b), as revealed by ESI-MS (Supplementary Fig. 15). Compared with the water-only single-phase system (Fig. 4a and Supplementary Fig. 16), the interphase-assisted approach produced a narrower ligand distribution at low free ligand to Au_{25} ratios end (i.e., p -MBA: $\text{Au}_{25}(\text{p-MBSA})_{18} = 0 - 6$), demonstrating that the modulated mass transfer by the water-EA two-phase design enables a precisely controlled ligand exchange process. Similar narrow ligand distribution can be found at the high p -MBA: $\text{Au}_{25}(\text{p-MBSA})_{18}$ ratio = 100 or above. By contrast, the ligand distribution turns relatively broad at moderate p -MBA: $\text{Au}_{25}(\text{p-MBSA})_{18}$ ratios ranging from 6 to 100. Therefore, this study also unambiguously identifies the ligand distribution limits in the ligand-exchange reactions. It should be mentioned that the single-phase approach, most likely due to its less effective control over ligand exchange kinetics, produces bi-thiolate-protected $\text{Au}_{25}(\text{p-MBSA})_{18-n}(\text{p-MBA})_n$ in a much broader ligand distribution almost through the entire p -MBA: $\text{Au}_{25}(\text{p-MBSA})_{18}$ ratio range (Fig. 4a).

Apart from phenyl ligands like p -MBA and p -MBSA, this interphase-assisted approach is also applicable for driving the ligand

exchange reactions with alkyl ligands like MPA and MHA. By dissolving MPA or MHA into the EA solution at a MPA or MHA: $\text{Au}_{25}(\text{p-MBSA})_{18}$ ratio of 200, the interphase mass transfer method is able to induce the ligand-exchange reaction, giving rise to a yield of >90% in terms of the ligand-exchanged Au_{25} NCs (Supplementary Fig. 17a, c). ESI-MS was also employed to characterize the ligand distribution on the surface of ligand-exchanged Au_{25} NCs, which manifested formula of $\text{Au}_{25}(\text{p-MBSA})_{6-16}(\text{MPA})_{2-12}$ for MPA and $\text{Au}_{25}(\text{p-MBSA})_{6-11}(\text{MHA})_{7-12}$ for MHA exchange clusters (Supplementary Fig. 17b, d). The zoomed-in ESI-MS spectra and isotope patterns can be found in Supplementary Figs. 18 and 19.

Besides functionalizing $\text{Au}_{25}(\text{p-MBSA})_{18}$ with phenyl or alkyl thiolate terminated by carboxylic groups, ligands terminated by other function groups can also be anchored on the surface of Au_{25} through the interphase-assisted ligand exchange strategy. Hydrophilic ligands with neutral (e.g., nitrothiophenol (NTP)) and mercaptophenol (MP)) and positive (e.g., aminothiophenol (*p*-ATP)) charges, as well as hydrophobic ligands (e.g., thiophenol (TP)), can be deployed to furnish the surface of $\text{Au}_{25}(\text{p-MBSA})_{18}$. As shown by the ESI-MS spectra (Fig. 5), NTP, *p*-ATP, and MP showed similar exchange extent ($\text{Au}_{25}(\text{p-MBSA})_{18-14}(\text{NTP})_{0-4}$, $\text{Au}_{25}(\text{p-MBSA})_{18-14}(\text{p-ATP})_{0-4}$, and $\text{Au}_{25}(\text{p-MBSA})_{18-14}(\text{MP})_{0-4}$), most probably due to their similar aromatic

structures and hydrophilicities (Supplementary Figs. 20–22). In contrast, the hydrophobic TP replaced up to 9 *p*-MBSA ligands. Of note, TP-exchanged Au_{25} NCs by this way exhibited notable amphiphilicity, enhancing clusters' solubility in the interfacial regions of EA-water system. Such enhanced solubility can further promote ligand exchange reaction and result in a broader ligand distribution in the final product (Supplementary Fig. 23).

Importantly, this interphase-assisted ligand exchange approach also exhibits general applicability to other size and ligand-protected Au NCs, such as $\text{Au}_{22}(\text{GSH})_{18}$ (GSH: glutathione) and $\text{Au}_{44}(\text{p-MBA})_{26}$. Structural integrity is effectively maintained during ligand exchange, allowing the introduction of diverse ligands onto the Au NCs' surface (Supplementary Figs. 24 and 25). These findings highlight the versatility of this strategy for creating structurally robust, ligand-tailored metal NCs that hold promise for broad functional applications in bioimaging, catalysis, and many other fields.

Given the distinct ability of this method to control the ligand exchange process (Fig. 4b), we expect that by varying the feeding ratio of incoming thiol ligands, it is possible to produce a series of bi-ligand protected Au NCs with tailored properties. This capability will enable deeper exploration of ligand effects on nanoparticle properties and their applications, particularly in the biomedicine fields.

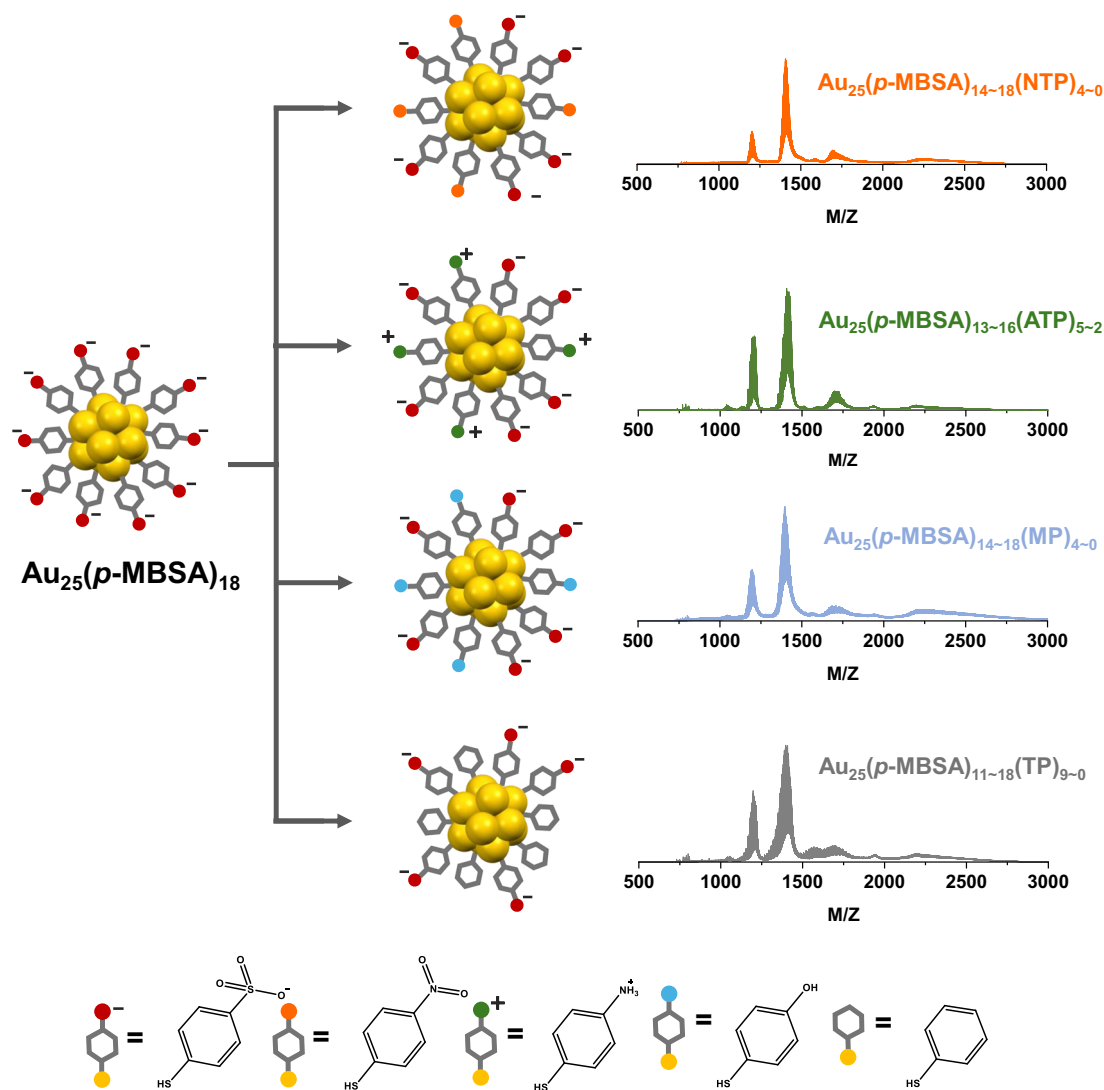


Fig. 5 | Versatility of interphase mass transfer-assisted ligand exchange method. Ligand exchange of $\text{Au}_{25}(\text{p-MBSA})_{18}$ with various ligands containing different functional groups.

Ligand effect on biodistribution

Understanding how surface ligands influence the bio-distribution and organ accumulation of NPs is essential for their successful application in bio-imaging and targeted drug delivery⁴⁴. The surface charge, largely imparted by functional groups of protecting ligands, has been shown critical for biological behavior of NPs^{7,45}. Previous reports have indicated that NPs with zwitterionic coatings can prohibit protein corona formation, exhibiting longer blood circulation times. It is also suggested that NPs with zwitterionic surface have distinctly different biodistribution profiles compared to those with purely anionic or cationic charges⁴⁶. However, there is still a lack of precise understanding on the mechanism of zwitterionic coatings affecting the biodistribution profiles, due to the inherent challenges of manipulating conventional NPs at the atomically precise level.

Leveraging the interphase-assisted ligand exchange method developed in this study, we are able to fine tune the surface charge of Au₂₅ NCs by precisely locating oppositely charged ligands like *p*-ATP and *p*-MBSA on cluster surface. Experimentally, positively charged *p*-ATP was accommodated in EA phase, while Au₂₅(*p*-MBSA)₁₈ NCs were dissolved in aqueous phase. The coverage of *p*-ATP can be simply tuned by the feeding ratio of *p*-ATP: Au₂₅(*p*-MBSA)₁₈. This capability of precise surface engineering allowed us to explore, at a molecular level, how zwitterionic coatings affect biodistribution of metal NPs. In particular, by modifying the surface composition of Au NCs, we aimed to shed light on why zwitterionic ligands reduce protein interactions and alter organ accumulation in vivo.

To this end, we synthesized a series of bi-ligand Au NCs using different *p*-ATP feeding ratios (*p*-ATP: Au₂₅(*p*-MBSA)₁₈ = 4, 20, 50, 150). The resulting bi-ligand Au NCs, Au₂₅(*p*-MBSA)₁₅(*p*-ATP)₃, Au₂₅(*p*-MBSA)₁₄(*p*-ATP)₄, Au₂₅(*p*-MBSA)₁₀(*p*-ATP)₈ and Au₂₅(*p*-MBSA)₉(*p*-ATP)₉ (the number of *p*-ATP here denotes the average number on the surface of Au NCs), were identified by NMR spectra (Supplementary Figs. 26–29). These bi-ligand protected Au NCs displayed a gradual positive shift in surface charge as the concentration of *p*-ATP increased (Supplementary Fig. 30). This positive shift in surface charge is also in good accordance with successive incorporation of positive *p*-ATP ligands into the protecting shell of Au₂₅ NCs.

It is well-established that Au₂₅(SR)₁₈ NCs exhibit strong NIR-II fluorescence upon appropriate excitation. To assess any possible ligand effects on fluorescence, we compared the concentration-dependent fluorescence profiles of Au₂₅(*p*-MBSA)₁₈ and *p*-ATP/*p*-MBSA co-protected Au NCs in vitro (Fig. 6a). Quantitative fluorescence analyses revealed comparable emission intensities among all tested NCs at equivalent concentrations (Fig. 6b), indicating that ligand modifications did not significantly alter intrinsic fluorescence properties. This result provided a robust basis for subsequent comparative investigations of in vivo biodistribution.

We utilized real-time NIR-II imaging (808 nm excitation) to monitor the systemic distribution of Au₂₅ NCs in mice. The *p*-ATP/*p*-MBSA co-protected Au NCs exhibited dynamic trafficking to key organs (liver, spleen, kidneys, and bladder), followed by effective renal clearance (Fig. 6c). Notably, ligand-dependent shifts in biodistribution were observed. The negatively charged Au₂₅(*p*-MBSA)₁₈ NCs, bearing exclusively anionic carboxylate groups, preferentially accumulated in the liver and spleen. Conversely, increasing *p*-ATP ligand ratios progressively redirected NC distribution from hepatic and splenic retention toward renal elimination. At 3 h post-injection, bladder fluorescence signals from Au₂₅(*p*-MBSA)₁₈ were negligible compared to *p*-ATP-modified counterparts. By 6 h, higher proportions of *p*-ATP ligands correlated with enhanced bladder fluorescence and reduced hepatic retention (Fig. 6d–e), suggesting improved renal clearance efficiency.

Ex vivo NIR-II imaging of harvested organs further validated these observations, clearly showing reduced accumulation in liver and spleen and enhanced renal excretion due to zwitterionic *p*-ATP modification (Fig. 6f–6i). To quantitatively assess in vivo clearance, Au

concentrations in metabolic outputs were measured via inductively coupled plasma mass spectrometry (ICP-MS). At 24 h post-injection, the *p*-ATP-modified Au NCs (Au NCs: *p*-ATP = 1:150) exhibited approximately 20% injected dose (ID) urinary excretion, twice that observed for Au₂₅(*p*-MBSA)₁₈NCs (Fig. 6j and 6k). Fecal Au excretion was consistently ~5% ID across all groups, further confirming the *p*-ATP-mediated enhancement of renal elimination.

To further investigate the role of surface charge and functional groups, we performed a control experiment by introducing hydroxyl (-OH) groups instead of -NH₂ on the surface of Au₂₅(*p*-MBSA)₁₈ (Supplementary Fig. 31a–e). Interestingly, unlike the -NH₂-modified Au NCs (i.e., Au₂₅(*p*-MBSA)_{18-n}(*p*-ATP)_n), the -OH modification (i.e., Au₂₅(*p*-MBSA)_{18-n}(MP)_n) did not significantly alter the accumulation of Au NCs from the liver to the kidneys. Instead, the -OH-modified Au NCs exhibited a more even distribution throughout the body, without a pronounced shift toward renal clearance. This finding suggests that the -NH₂ group plays a critical role in directing Au NCs towards kidney excretion, likely due to its positive charge and ability to form zwitterionic structures at physiological pH (pK_a of -NH₂ is 10.46)⁴⁷. The -OH group, being neutral, did not produce the same effect, further emphasizing the importance of surface charge in determining biodistribution.

To ensure that the observed biodistribution trends were not influenced by any differences in colloidal stability, we next examined the stability of the partially ligand-exchanged Au₂₅ NCs under various pH and ionic strength conditions. Four bi-ligand-protected Au NCs were incubated in pH 4 (sustained by sodium tetraborate buffer), pH 7 (PBS buffer), pH 9 (potassium hydrogen phthalate buffer), and high-salt solution (100 mM NaCl) for 24 h. UV–vis absorption spectra recorded within 24 h (Supplementary Figs. 32, 33) showed no significant shifts or peak broadening for any of the tested NCs in above-mentioned conditions, indicating that all tested Au NCs remain colloidally stable across the concerned pH range and at physiological ionic strength. Thus, the Au₂₅ NCs retain their structural integrity under physiologically relevant conditions, and the variations in organ uptake we observed can be attributed to the intended ligand shell differences rather than any instability. Coupled with the rapid renal clearance of these NCs within 24 h post-injection, these stability results support the reliability of our in vivo findings and affirm the suitability of the ligand-engineered Au₂₅ NCs for biological applications.

These results underscore the importance of surface charge in dictating biodistribution of bioactive nanoparticles. The zwitterionic configuration of the Au₂₅(*p*-MBSA)_{18-n}(*p*-ATP)_n NCs, balancing positive and negative charges, likely reduces protein adsorption, minimizes liver and spleen accumulation, and facilitates renal clearance. This study provides useful insights into how ligand design, particularly the choice of terminal functional groups, can be optimized for specific biomedical applications, such as targeted imaging and drug delivery.

In summary, we developed an interphase mass transfer assisted ligand exchange strategy for precise surface engineering of atomically precise metal NCs. This method effectively utilizes mass transfer resistance between partially miscible phases to regulate free ligand concentration, minimizing side etching reaction and thus allowing for high-yield, structure-preserving ligand exchange reaction on parent metal NCs. Using Au₂₅(*p*-MBSA)₁₈ as a model system, we successfully introduced a wide spectrum of ligands with varied charge (i.e., negative, neutral, and positive), ligand body structure (i.e., phenyl and alkyl), and terminal groups (e.g., carboxylic, sulfonic, hydroxyl, and nitro), to create bi-thiolate-protected Au NCs with controlled ligand distributions. A series of *p*-ATP/*p*-MBSA co-protected Au₂₅ NCs manufactured via this method demonstrated a clear shift in accumulation from the liver and spleen toward the kidneys with increasing amounts of *p*-ATP on the surface of Au₂₅ NCs, shedding fundamental light on ligand effects of metal NPs on their biological fate. By systematically tuning the surface charge through ligand engineering, we can design NCs with optimized biodistribution profiles for applications in bio-

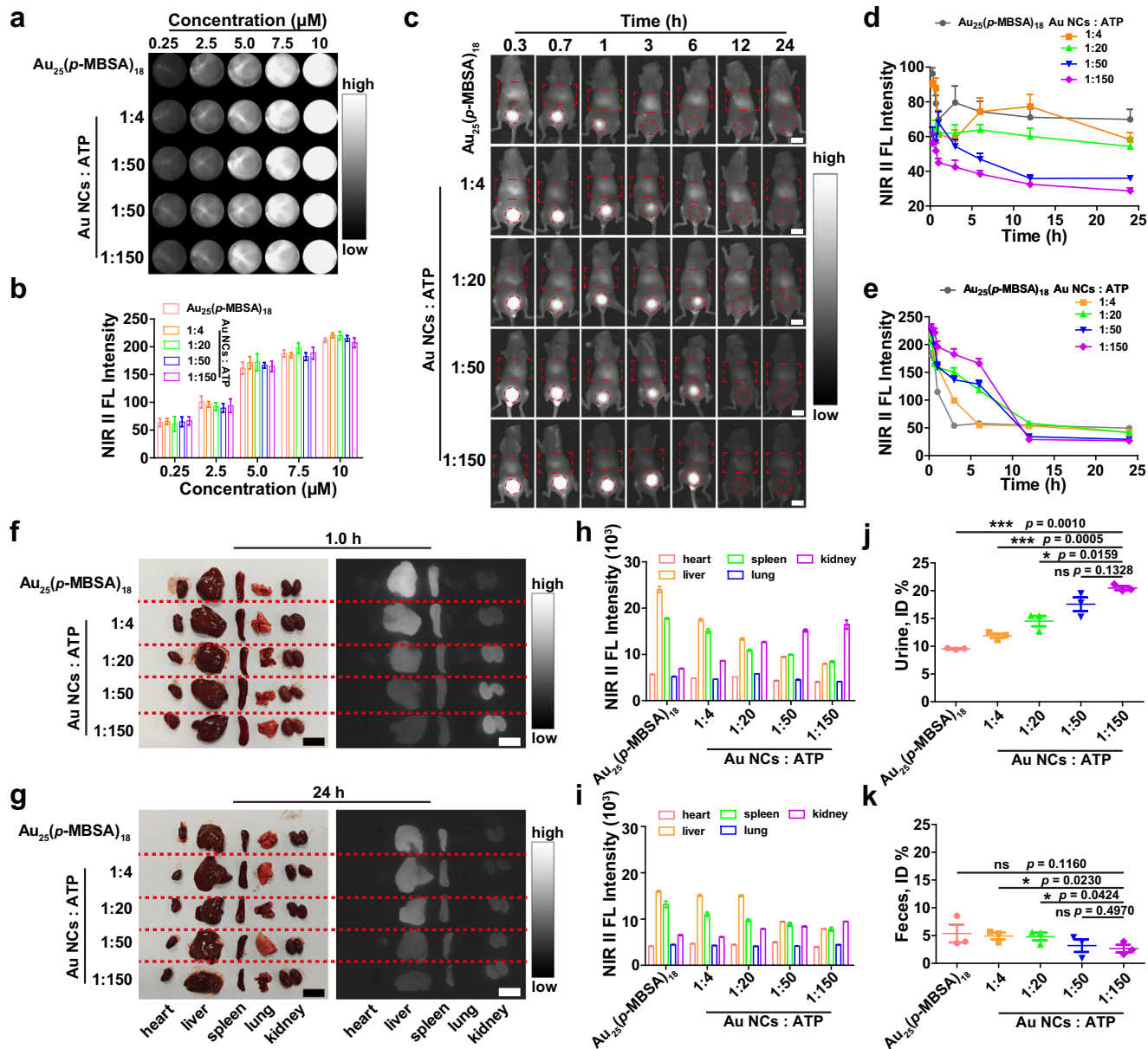


Fig. 6 | Precise ligand engineering promoted bio-distribution of Au₂₅ NCs. **a** NIR II fluorescence images and **b** corresponding quantification of Au₂₅(*p*-MBSA)₁₈, Au₂₅(*p*-MBSA)_{18-*n*}(*p*-ATP)_{*n*} (synthesized via the interphase-assisted ligand exchange at molar ratios of *p*-ATP: Au₂₅(*p*-MBSA)₁₈ = 4, 20, 50, and 150) at various concentrations. The assay was repeated three times for each sample group. **c** NIR II imaging at different time points monitoring the metabolism of Au₂₅(*p*-MBSA)₁₈, Au₂₅(*p*-MBSA)_{18-*n*}(*p*-ATP)_{*n*} (at molar ratios of *p*-ATP: Au₂₅(*p*-MBSA)₁₈ = 4, 20, 50, and 150) with the concentration of 10 μM in the liver and bladder. Scale bar, 1 cm. The

NIR II fluorescence quantification in **d** liver and **e** bladder of mice over time. Three mice per group (independent experiments). NIR II fluorescence imaging of major organs at **f** 1 h and **g** 24 h post-injection of different Au NCs (10 μM), along with their corresponding fluorescence quantification at **h** 2 h and **i** 24 h. Scale bar, 1 cm. Three mice per group (independent experiments). Au content in **j** urine and **k** feces collected over 24 h post-injection, quantified by ICP-MS. Three mice per group (independent experiments). All the data are shown as mean ± SD (*n* = 3 mice per group). ns: not significant, **p* < 0.05, ***p* < 0.01, ****p* < 0.001 (Student's *t*-test).

imaging, targeted drug delivery, and many other sectors of nanomedicine. This work not only offers a facile and versatile method for atomically precise engineering of cluster surface but also affords fundamental insights into the ligand exchange and etching reaction of metal NCs at molecular level, facilitating the rational design of functional nanomaterials for targeted bio-imaging and drug delivery at the same resolution.

Methods

Animal ethics

Female BALB/c mice (6 weeks old, *n* = 45) were sourced from the Guangdong Medical Laboratory Animal Center under standardized

conditions. Female mice were utilized to avoid aggressive interactions inherent to males of this immunodeficient strain. All animal experiments were approved by the Institutional Animal Care and Use Committee of Southern University of Science and Technology (Approval ID: SUSTech-SL2024022812). These experiments were conducted in strict compliance with relevant laws and ethical standards as specified in the Guide for the Care and Use of Laboratory Animals by the National Institutes of Health.

Synthesis of Au NCs protected by *p*-MBSA and *p*-MBA

The synthesis protocol was designed based on the CO-reduction method developed by our group in 2020⁴⁰. In a typical synthesis,

ligands (i.e., *p*-MBSA or *p*-MBA) (6.5 mL, 50 mM), NaOH (0.25 mL, 1 M), and an aqueous solution of HAuCl₄ (7.5 mL, 20 mM) were added into 134 mL ultrapure water in sequence. After stirring for about 5 min, NaOH solution (1 M) was used to adjust the pH of the solution to 10.8, and the solution was continued stirring vigorously for 30 min. After that, one bar of CO was bubbled into the solution for 2 min. Immediately afterward, the reaction bottle was tightly sealed using a rubber septum and secured with parafilm to ensure an airtight environment, preventing any leakage of CO gas or ingress of oxygen. The sealed bottle was then carefully placed on a magnetic stirrer in a maintained ambient temperature (−25 °C) and protected from direct exposure to sunlight to prevent undesired photochemical reactions. The raw products were collected after reacting for 6 days with stirring at 500 rpm at room temperature and followed by a rotary evaporation to concentrate the mother solution. Finally, the products were precipitated by introducing 3-fold volume of ethanol and washed by dimethylformamide for 3 times. The purified Au NCs was dissolved in 15 mL of ultrapure water (−0.3 mM) then used to conduct ligand exchange reactions.

Etching reaction kinetics investigation

Etching reaction was carried out by mixing Au₂₅(*p*-MBSA)₁₈ with *p*-MBA in aqueous solution. The absorbance of Au₂₅ NCs was continuously monitored at 698 nm, as the concentration of Au₂₅ NCs follows Beer-Lambert's law:

$$A = \varepsilon \times c \times l$$

where *A* is the absorbance; ε is the molar absorptivity; *c* is the concentration of Au₂₅ NCs, and *l* is the path length of the cuvette. The etching reaction rates were calculated by differentiating the absorbance data over time, and the logarithmic plots were fitted using linear regression to extract the reaction orders. Different concentrations of Au₂₅(*p*-MBSA)₁₈ and *p*-MBA were tested to examine their effect on the etching kinetics.

Ligand exchange reaction kinetics investigation

Ligand exchange reaction was also carried out by mixing Au₂₅(*p*-MBSA)₁₈ with *p*-MBA in aqueous solution like the etching reaction. The ligand exchange reaction was terminated at specific time intervals by precipitating Au NCs using ethanol at three times the volume of the reaction solution, supplemented by the addition of a concentrated NaCl solution to achieve a final NaCl concentration of 1 M. The precipitation was washed by DMF for three times to eliminate the free ligands. And then the product of bi-ligand protected Au₂₅NCs were redissolved in D₂O and tested ¹H spectra in NMR to determine the concentrations of individual ligands. The ligand exchange reaction rates were calculated by differentiating the concentration of exchanged Au NCs over time, and the logarithmic plots were fitted using linear regression to extract the reaction orders.

Two-phase ligand exchange reaction

The two-phase ligand exchange reaction was conducted by simply mixing an aqueous phase contained Au NCs and an organic phase contained desired thiol ligands. The aqueous phase is 2 mL of 0.025 mM aqueous solution of purified Au₂₅(SR)₁₈, adjusted precisely to pH 7 using dilute CH₃COOH solutions. The organic phase is prepared by dissolving certain amount of ligands (e.g., *p*-MBA, MPA, MHA and so on.) in 2 mL of EA. The two phases are mixed by vigorous stirring at 1000 rpm for 1 h. The product in aqueous phase was collected by separation after the stratification for further characterization.

Single-phase ligand exchange

A certain amount of Au NCs (e.g., 0.025 mM) and ligands were added into ultrapure water together. After 1 h stirring, the suspension is collected and purified by ultracentrifuge to remove excess free ligands.

Calculation of etching kinetics in two phase ligand exchange

To compare the etching kinetics across two-phase ligand exchange reactions with different organic phases. We monitor the time-dependent absorbance of Au₂₅ NCs at 698 nm in UV-vis spectra, which can be transferred to molar concentration using Beer-Lambert's law, and then used to calculate the etching kinetics of Au₂₅ NCs.

Calculation of ligand exchange kinetics in two phase ligand exchange

To compare the ligand exchange kinetics across two-phase ligand exchange reactions with different organic phases. We collect the ligand exchange product synthesized via different organic two-phase ligand exchange reaction at the same time, 30 min. The maximum number of exchanged *p*-MBA ligands on the Au NC surface, represented by the maximum *n* in Au₂₅(*p*-MBSA)_{18-*n*}(*p*-MBA)_{*n*}, was used to calculate ligand exchange kinetics, with *n* determined by ESI-MS spectra (Supplementary Figs. 2–6).

Animal experiments

Female BALB/c mice, aged 6 weeks, were obtained from the Guangdong Medical Laboratory Animal Center. All animal experiments were approved by the Institutional Animal Care and Use Committee of Southern University of Science and Technology (Approval ID: SUS-Tech-SL2024022812). These experiments were conducted in strict compliance with relevant laws and ethical standards as specified in the Guide for the Care and Use of Laboratory Animals by the National Institutes of Health.

Bioimaging

To investigate the in vivo distribution of different NCs in mice, we administered Au₂₅(*p*-MBSA)₁₈, Au₂₅(*p*-MBSA)_{18-*n*}(*p*-ATP)_{*n*} (synthesized via water-EA two-phase ligand exchange reaction at ratios of *p*-ATP: Au₂₅(*p*-MBSA)₁₈ = 4, 20, 50, and 150, where *p*-ATP denotes *p*-aminothiophenol), and Au₂₅(*p*-MBSA)_{18-*n*}(MP)_{*n*} (synthesized via water-EA two-phase ligand exchange reaction at ratios of MP: Au₂₅(*p*-MBSA)₁₈ = 20 and 150, where MP denotes mercaptophenol) via tail vein injection. The distribution of these NCs was monitored at various time points using a NIR II fluorescence imager (NIROPTICS, Series III 900/1700) with a laser power of 5 W (approximately −20 mW cm^{−2}). To enhance our monitoring of the NCs' distribution, we performed ex vivo imaging of the 1 h and 24 h post-injection. To monitor the metabolism of Au NCs, we collected urine and feces 24 h after the injection of Au NCs using metabolic cages, during which the mice were subjected to a 2-h water deprivation period. The Au content was then quantified by ICP-MS (Agilent, 7900).

Statistical analysis

Data are presented as means ± standard deviation (SD). In vivo experiments were performed independently in three separate trials, with each group comprising at least three replicates. Statistical analyses were conducted using GraphPad Prism 8 software, employing Student's *t*-tests analysis of variance. A *p*-value of less than 0.05 was considered statistically significant in this study.

Materials characterization

UV-vis absorption spectra were recorded with a Shimadzu UV-1800 spectrometer. Electrospray ionization (ESI) mass spectra were obtained on a Bruker Micro TOF-Q system, with a sample injection velocity of 540 μL min^{−1}. The other parameters are as follows: dry gas, 2 L min^{−1} at 120 °C; *m/z* range, 100 – 6000; capillary voltage, 4 kV;

nebulizer, 0.4 bar; transfer time, 25 μ s. Nuclear magnetic resonance (NMR) analysis was conducted on a Bruker Avance DMX 500 spectrometer operating at 500.13 MHz for ^1H . Zeta potential was measured on Malvern Zetasizer Pro. The bioimaging was conducted using a NIR-II fluorescence imager, NIROPTICS, Series III 900/1700, with a laser power of 5 W.

Reporting summary

Further information on research design is available in the Nature Portfolio Reporting Summary linked to this article.

Data availability

All data underlying this study are available from the corresponding author upon request. Source data are provided with this paper.

References

- Zhang, J. et al. Stimuli-responsive nanoparticles for controlled drug delivery in synergistic cancer immunotherapy. *Adv. Sci.* **9**, 2103444 (2022).
- Song, X. et al. A new class of NIR-II gold nanocluster-based protein biolabels for in vivo tumor-targeted imaging. *Angew. Chem. Int. Ed.* **60**, 1306–1312 (2021).
- Chen, Y., Xianyu, Y. & Jiang, X. Surface modification of gold nanoparticles with small molecules for biochemical analysis. *Acc. Chem. Res.* **50**, 310–319 (2017).
- Zhang, J. et al. Weakly ionized gold nanoparticles amplify immunoassays for ultrasensitive point-of-care sensors. *Sci. Adv.* **10**, eadn5698 (2024).
- Hua, Y. et al. Water-soluble Au₂₅ clusters with single-crystal structure for mitochondria-targeting radioimmunotherapy. *ACS Nano* **17**, 7837–7846 (2023).
- Ju, Y., Kim, C.-J. & Caruso, F. Functional ligand-enabled particle assembly for bio–nano interactions. *Acc. Chem. Res.* **56**, 1826–1837 (2023).
- Elci, S. G. et al. Surface charge controls the suborgan biodistributions of gold nanoparticles. *ACS Nano* **10**, 5536–5542 (2016).
- Shichibu, Y. et al. Extremely high stability of glutathionate-protected Au₂₅ clusters against core etching. *Small* **3**, 835–839 (2007).
- Zhang, B., Chen, J., Cao, Y., Chai, O. J. H. & Xie, J. Ligand design in ligand-protected gold nanoclusters. *Small* **17**, 2004381 (2021).
- Matus, M. F. & Häkkinen, H. Understanding ligand-protected noble metal nanoclusters at work. *Nat. Rev. Mater.* **8**, 372–389 (2023).
- Yao, Q. et al. Supercrystal engineering of atomically precise gold nanoparticles promoted by surface dynamics. *Nat. Chem.* **15**, 230–239 (2023).
- Pedraza-Tardajos, A. et al. Direct visualization of ligands on gold nanoparticles in a liquid environment. *Nat. Chem.* **16**, 1278–1285 (2024).
- Pyo, K. et al. Highly luminescent folate-functionalized Au₂₂ nanoclusters for bioimaging. *Adv. Health. Mater.* **6**, 1700203 (2017).
- Baghdasaryan, A. et al. Intratumor injected gold molecular clusters for NIR-II imaging and cancer therapy. *Proc. Natl. Acad. Sci. USA* **121**, e2318265121 (2024).
- Yang, G. et al. Phosphorylation of NIR-II emitting Au nanoclusters for targeted bone imaging and improved rheumatoid arthritis therapy. *Aggregate* **5**, e435 (2024).
- Kang, X., Chong, H. & Zhu, M. Au₂₅(SR)₁₈: the captain of the great nanocluster ship. *Nanoscale* **10**, 10758–10834 (2018).
- Chakraborty, I. & Pradeep, T. Atomically precise clusters of noble metals: emerging link between atoms and nanoparticles. *Chem. Rev.* **117**, 8208–8271 (2017).
- Du, B., Yu, M. & Zheng, J. Transport and Interactions of Nanoparticles in the Kidneys. *Nat. Rev. Mater.* **3**, 358–374 (2018).
- Jin, R. Atomically precise metal nanoclusters: stable sizes and optical properties. *Nanoscale* **7**, 1549–1565 (2015).
- Wan, X.-K. et al. A near-infrared-emissive Alkynyl-protected Au₂₄ nanocluster. *Angew. Chem. Int. Ed.* **54**, 9683–9686 (2015).
- Pan, X. et al. Enzyme-mimic catalytic activities and biomedical applications of noble metal nanoclusters. *Nanoscale* **16**, 8196–8215 (2024).
- Chen, X., Ren, X. & Gao, X. Peptide or protein-protected metal nanoclusters for therapeutic application. *Chin. J. Chem.* **40**, 267–274 (2022).
- Du, Y., Sheng, H., Astruc, D. & Zhu, M. Atomically precise noble metal nanoclusters as efficient catalysts: a bridge between structure and properties. *Chem. Rev.* **120**, 526–622 (2020).
- Yao, Q., Yuan, X., Chen, T., Leong, D. T. & Xie, J. Engineering functional metal materials at the atomic level. *Adv. Mater.* **30**, e1802751-n/a (2018).
- Hossain, S. et al. Atomically precise thiolate-protected gold nanoclusters: current status of designability of the structure and physicochemical properties. *Aggregate* **4**, e255 (2023).
- Takano, S., Hirai, H., Muramatsu, S. & Tsukuda, T. Hydride-doped gold superatom (Au₉H)²⁺: synthesis, structure, and transformation. *J. Am. Chem. Soc.* **140**, 8380–8383 (2018).
- Li, S. et al. Atom-precise modification of silver(I) thiolate cluster by shell ligand substitution: a new approach to generation of cluster functionality and chirality. *J. Am. Chem. Soc.* **140**, 594–597 (2018).
- Negishi, Y. et al. Magic-numbered aun clusters protected by glutathione monolayers (n = 18, 21, 25, 28, 32, 39): isolation and spectroscopic characterization. *J. Am. Chem. Soc.* **126**, 6518–6519 (2004).
- Kurashige, W. et al. Au₂₅ clusters containing unoxidized tellurolates in the ligand shell. *J. Phys. Chem. Lett.* **5**, 2072–2076 (2014).
- Yuan, X. et al. Balancing the rate of cluster growth and etching for gram-scale synthesis of thiolate-protected Au₂₅ nanoclusters with atomic precision. *Angew. Chem. Int. Ed.* **53**, 4623–4627 (2014).
- Zhang, S. Property tailoring of gold clusters via surface engineering and supramolecular assembly. In: *Atomically Precise Metal Clusters* (2024).
- Huang, Z., Ishida, Y., Narita, K. & Yonezawa, T. Kinetics of cationic-ligand-exchange reactions in Au₂₅ nanoclusters. *J. Phys. Chem. C* **122**, 18142–18150 (2018).
- Zeng, C., Liu, C., Pei, Y. & Jin, R. Thiol ligand-induced transformation of Au₃₈(SC₂H₄Ph)₂₄ to Au₃₆(SPh-t-Bu)₂₄. *ACS Nano* **7**, 6138–6145 (2013).
- Zeng, C., Chen, Y., Das, A. & Jin, R. Transformation chemistry of gold nanoclusters: from one stable size to another. *J. Phys. Chem. Lett.* **6**, 2976–2986 (2015).
- Dong, H., Liao, L. & Wu, Z. Two-way transformation between fcc- and Nonfcc-structured gold nanoclusters. *J. Phys. Chem. Lett.* **8**, 5338–5343 (2017).
- Kurashige, W., Yamaguchi, M., Nobusada, K. & Negishi, Y. Ligand-induced stability of gold nanoclusters: thiolate versus selenolate. *J. Phys. Chem. Lett.* **3**, 2649–2652 (2012).
- Yao, C. et al. Synthesis of fluorescent phenylethanethiolated gold nanoclusters via pseudo-AGR method. *Nanoscale* **7**, 16200–16203 (2015).
- Zhou, M. & Song, Y. Origins of visible and near-infrared emissions in [Au₂₅(SR)₁₈]⁻ nanoclusters. *J. Phys. Chem. Lett.* **12**, 1514–1519 (2021).
- Zhai, X.-J. et al. Luminescence modulation of ultrasmall gold clusters by aromatic ligands. *Nano Res.* **16**, 11366–11374 (2023).
- Zhang, B., Wu, Z., Cao, Y., Yao, Q., Xie, J. Ultrastable hydrophilic gold nanoclusters protected by sulfonic thiolate ligands. *J. Phys. Chem. C* **125**, 489–497 (2020).
- Dass, A., Holt, K., Parker, J. F., Feldberg, S. W. & Murray, R. W. Mass spectrometrically detected statistical aspects of ligand populations in mixed monolayer Au₂₅L₁₈ nanoparticles. *J. Phys. Chem. C* **112**, 20276–20283 (2008).

42. Cao, Y. et al. Control of single-ligand chemistry on thiolated Au₂₅ nanoclusters. *Nat. Commun.* **11**, 5498 (2020).
43. Cao, Y. et al. Revealing the etching process of water-soluble Au₂₅ nanoclusters at the molecular level. *Nat. Commun.* **12**, 3212 (2021).
44. Ansari, A. A., Parchur, A. K. & Chen, G. Surface modified lanthanide upconversion nanoparticles for drug delivery, cellular uptake mechanism, and current challenges in NIR-driven therapies. *Coord. Chem. Rev.* **457**, 214423 (2022).
45. Soo Choi, H. et al. Renal clearance of quantum dots. *Nat. Biotechnol.* **25**, 1165–1170 (2007).
46. Hamadani, C. M., Goetz, M. J., Mitragotri, S. & Tanner, E. E. L. Protein-avoidant Ionic Liquid (PAIL)-coated nanoparticles to increase bloodstream circulation and drive biodistribution. *Sci. Adv.* **6**, eabd7563 (2020).
47. Perrin, D. D. *Ionisation Constants of Inorganic Acids and Bases in Aqueous Solution* (Elsevier, 2016).

Acknowledgements

The authors acknowledge the financially supported by the Ministry of Education, Singapore (A-8000054-01-00, A-8002581-00-00), National Natural Science Foundation of China (92461304, 22371204), and the Fundamental Research Funds for the Central Universities.

Author contributions

J.X., Q.Y. and M.Z. supervised the experimental work; J.X., Q.Y., M.Z., B.Z., and X.F. conceived the idea and design the experiment; B.Z., X.F. and X.S. carried out the experiments and characterizations; All authors contributed to manuscript writing.

Competing interests

The authors declare no competing interests.

Additional information

Supplementary information The online version contains supplementary material available at <https://doi.org/10.1038/s41467-026-68345-z>.

Correspondence and requests for materials should be addressed to Moshuqi Zhu, Qiaofeng Yao or Jianping Xie.

Peer review information *Nature Communications* thanks Yohei Ishida, and the other anonymous, reviewer(s) for their contribution to the peer review of this work. A peer review file is available.

Reprints and permissions information is available at <http://www.nature.com/reprints>

Publisher's note Springer Nature remains neutral with regard to jurisdictional claims in published maps and institutional affiliations.

Open Access This article is licensed under a Creative Commons Attribution-NonCommercial-NoDerivatives 4.0 International License, which permits any non-commercial use, sharing, distribution and reproduction in any medium or format, as long as you give appropriate credit to the original author(s) and the source, provide a link to the Creative Commons licence, and indicate if you modified the licensed material. You do not have permission under this licence to share adapted material derived from this article or parts of it. The images or other third party material in this article are included in the article's Creative Commons licence, unless indicated otherwise in a credit line to the material. If material is not included in the article's Creative Commons licence and your intended use is not permitted by statutory regulation or exceeds the permitted use, you will need to obtain permission directly from the copyright holder. To view a copy of this licence, visit <http://creativecommons.org/licenses/by-nc-nd/4.0/>.

© The Author(s) 2026